Sustainable Energy & Fuels

ROYAL SOCIETY OF CHEMISTRY

PAPER

View Article Online
View Journal

Cite this: DOI: 10.1039/d5se01348h

Conversion of novel bimetallic metal organic frameworks into hierarchically structured electrocatalysts for high performance hydrogen evolution

Dhouha Abid, Soressa Abera Chala, Rongji Liu, Tobias Rios-Studer, Christean Nickel, Sarra Rahali, Kevin Sowa, Galina Matveeva, Dandan Gao, Ute Kolb and Carsten Streb *

Developing economically viable and high-performance electrocatalysts for the hydrogen evolution reaction (HER) is crucial for achieving sustainable hydrogen production. However, achieving a combination of high catalytic activity and long-term stability remains a challenge. In this study, we report the development of hierarchically porous hollow Co–Ni doped carbon electrocatalysts synthesized *via* pyrolysis. The optimized CoNi-MOF@850 °C catalyst exhibited excellent HER kinetics in alkaline media, requiring only 148 mV overpotential at 10 mA cm^{-2} with a Tafel slope of 65 mV dec^{-1}, surpassing the monometallic Co and Ni catalysts and approaching the performance of the commercial Pt/C (95 mV, 43 mV dec^{-1}). Notably, when employed in an AEM electrolyzer, the CoNi-MOF@850 °C catalyst maintained ~96% potential retention over 100 h at 200 mA cm^{-2}, demonstrating an exceptional stability. The synergistic interaction between Co and Ni, combined with the hierarchical porous structure, enhances electronic conductivity, increases active site density, and facilitates efficient charge transfer, leading to the observed superior catalytic performance. These results demonstrate the potential of bimetallic MOF-derived catalysts as cost-effective and sustainable alternatives to noble-metal-based electrocatalysts for large-scale green hydrogen production technologies.

Received 12th October 2025
Accepted 9th December 2025

DOI: 10.1039/d5se01348h

rsc.li/sustainable-energy

Introduction

The growing global demand for clean and sustainable energy coupled with increasing environmental concerns has driven advancements in water-splitting technologies for hydrogen production.[1–5] Electrocatalytic water splitting is a sustainable method that offers high-purity hydrogen with potential for large-scale implementation.[6–10] It can serve as a crucial secondary energy carrier, enabling hydrogen to function as both a clean fuel and key chemical feedstock.

Powered by renewable energy, it provides a sustainable pathway for energy storage and industrial applications, thus supporting the global transition to a sustainable energy future.[11–14] However, electrochemical water splitting faces significant challenges, including efficiency losses, material incompatibility, and durability concerns owing to the electrochemical conditions, particularly when operating in alkaline media. At present, precious metals, such as platinum, remain the benchmark electrocatalysts for the HER owing to their high activity. However, their high cost, scarcity, and limited durability hinder their widespread use, necessitating the search for alternative, economical, and durable catalysts.[15,16] Recent advances in electrocatalysis have focused on non-noble 3d transition metal-based materials, such as cobalt, iron, manganese, and nickel, often as chalcogenides,[17,18] and phosphides,[19,20] which offer promising alternatives for HER. To assess these systems, metal organic framework (MOF) have received widespread attention as platform for developing efficient metal-based electrocatalysts.[21–24] MOFs offer several advantages, including high surface area, tunable structures, and the ability to incorporate a range of metal ions that can serve as active sites for the HER. In addition, MOFs can be converted by pyrolysis into porous carbon-based materials that exhibit electrical conductivity and enable electrocatalytic performance. When nitrogen-containing organic ligands are employed, controlled pyrolysis can lead to N-doped carbon matrices that feature electrical conductivity and provide stable support for dispersed metal species.[25,26] This improves electron transport to the active sites, ultimately enhancing the overall catalytic efficiency and stability of the HER. Although single-metal oxides derived from MOFs exhibit promising catalytic activity, their stability in alkaline media remains a challenge that limits their long-term performance. Additionally, single-

Department of Chemistry, Johannes Gutenberg University Mainz, Duesbergweg 10–14, Mainz 55128, Germany. E-mail: carsten.streb@uni-mainz.de

metal active sites often suffer from low density, restricted electronic interactions with reaction intermediates, and poor charge transfer kinetics.[27] To address these limitations, recent strategies have focused on developing bimetallic MOF-derived catalysts with enhanced stability and catalytic performance.[28–30] The introduction of a secondary metal into the MOF structure significantly improves the stability and activity of the catalyst under prolonged operational conditions. The synergy between the two metal species optimizes hydrogen adsorption, accelerates reaction kinetics, and reduces the overpotential required for the HER. Furthermore, bimetallic oxides exhibit high electrical conductivity, facilitating charge transfer at the electrode–electrolyte interface. Their improved structural integrity prevents degradation, thereby ensuring their long-term catalytic activity. These advantages make bimetallic metal oxides promising candidates for efficient and durable HER catalysis in alkaline environments. Paulraj et *al.* synthesized an MOF-derived CoNiP/CoNi/N-RGO nanosheet *via* pyrolysis at 450 °C, which exhibited excellent catalytic performance in a KOH electrolyte.[31] The catalyst achieved a low overpotential of 150 mV with a Tafel slope of 97 mV dec^{-1}, highlighting its efficiency for the HER in alkaline media. Similarly, Ehsan and colleagues employed MOF-74 as a template to prepare Co–Ni/carbon composite catalysts for the HER,[32] which demonstrated long-term stability for 24 h. This catalyst exhibited an overpotential of 174 mV and a Tafel slope of 106 mV dec^{-1}. Furthermore, Paulraj et *al.* developed a Ni–CoP/Co_2P catalyst,[33] that displayed remarkable HER activity, requiring an overpotential of 187 mV at a current density of 10 mA cm^{-2}, and a Tafel slope of 105 mV dec^{-1}.

While MOF-derived bimetallic systems show promise, a systematic study exploring the structure–performance relationship using novel mixed-ligand CoNi-MOF self-templates at optimized pyrolysis conditions is still lacking. Herein, we report the first synthesis and conversion of the novel M_2 (4,4′-bipyridine) (D-camphoric acid)$_2$ (M = Co, Ni, CoNi) frameworks into hierarchically structured mono and bimetallic carbon-based electrocatalysts. Various methods have been employed to explore the effects of the pyrolysis conditions, electronic interactions, doping effects, and structural properties on the catalytic properties of MOF-derived materials. Based on these studies, we demonstrate that the CoNi-MOF@850 °C catalyst achieves superior alkaline HER kinetics under large-scale due to synergistic electronic effects and enhanced active site density.

Results and discussion

The synthesis of porous CoNi nanoparticles embedded within a conductive carbon matrix was achieved through a two-step strategy, as illustrated in Fig. 1a. In the first step, bimetallic CoNi-MOF was synthesized *via* a self-assembly approach. This process involved the controlled coordination of Co and Ni metal ions with both the nitrogen-donor 4,4′-bipy and D-cam acid ligands, leading to the formation of highly ordered, crystalline 3D MOF structures. In the subsequent step, the as-synthesized MOF was subjected to pyrolysis under Ar atmosphere, during which the organic linkers were carbonized and the metal ions were simultaneously reduced to form a uniformly dispersed CoNi composite. To determine the optimal thermal conditions for the HER performance, monometallic Co-MOF and Ni-MOF

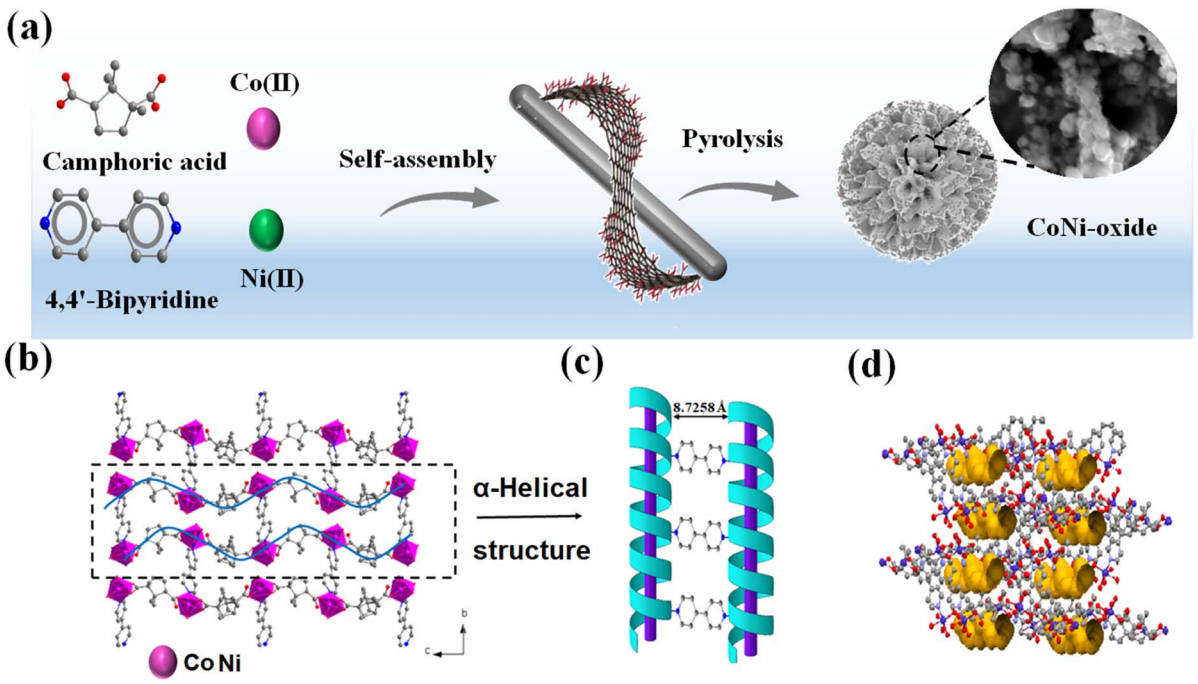

Fig. 1 (a) Schematic synthesis process of the mixed-ligand-based porous MOFs, (b) atomic arrangement along the crystallographic (b and c) plane highlighting the infinite left-right-handed double helices, and (c) 3D framework of the porous bimetallic MOF, and (d) accessible void volume represented by yellow channels.

were first synthesized as reference materials following the same procedure and subjected to pyrolysis at various temperatures (550–850 °C). These studies confirmed that pyrolysis temperature at 850 °C provides the best HER activity by enhancing its electronic conductivity and generating abundant active sites. Based on these findings, the bimetallic CoNi-MOF was subsequently pyrolyzed under the optimized conditions (850 °C) to yield the final CoNi-MOF@850 °C catalyst.

The synthesized MOFs were characterized before and after pyrolysis to study the structural and morphological evolution. The morphologies of the as-synthesized MOFs were investigated using scanning electron microscopy (SEM) (Fig. S1 and SI). Single-crystal X-ray diffraction (SCXRD) analysis revealed that MOF exhibited a porous 3D framework. Within the crystalline structure, the cobalt and nickel ions occupy the same positions within the structure. The asymmetric unit comprised two divalent metal ions, two deprotonated D-cam ligands, one 4,4′-bipy ligand, and four coordinated water molecules. Within this framework, each M^{2+} ($M = Co^{2+}/Ni^{2+}$) is six-coordinated in a $\{NO_5\}$ environment. Notably, the D-cam ligand exhibits two distinct chelating μ_2–η^1: η^1 and bridging η^1 modes, where the carboxylate groups (COO^-) bridge adjacent metal centers. This unique coordination arrangement resulted in the formation of infinite left-right-handed double helices along the [011] crystallographic direction (Fig. 1b). The 4,4′-bipy ligand acts as a μ_2:η^1:η^1 linker, connecting the two M(II) centers through its N_1 and N_2 donor atoms. These ligands are arranged alternately in an AB–AB fashion, effectively linking the helical chains and forming a pseudo-3D porous network with interconnected, straight channels (Fig. 1c).

The closest inter-helix distance within this structure was 8.7 Å. This 3D framework exhibits an unprecedented trinodal (2,1)-connected topology with a Schläfli symbol of $\{4^4.6^2\}$. The pore size was approximately 12.4 Å, and the unit cell volume of the framework was 1676 $Å^3$. The calculated porosity was 11.6% (143 $Å^3$), indicating a significant accessible void space within the unit cell for the guest solvent molecules (Fig. 1d). The synthesized MOFs were further analyzed using Powder X-ray diffraction (PXRD) (Fig. S2 and SI). The experimental bulk PXRD patterns closely matched the simulated patterns obtained from single-crystal analysis, confirming the phase purity of the materials. Minor variations in the peak intensities were likely due to differences in the preferred orientation of the crystallites and the presence of crystal defects within the samples.[34,35] The FT-Infrared (FT-IR) spectra of the MOFs, recorded at room temperature, confirmed that MOFs exhibited similar FT-IR spectra with characteristic peaks of the organic ligands (see Fig. S3a and SI). These findings were consistent with the structural features determined by X-ray crystallography. The thermogravimetric analysis (TGA) of the synthesized MOFs indicates various weight losses, which can be attributed to the loss of water molecules, the decomposition of organic ligands, and the formation of the metal oxide as a final residue.[35,36] For more details, see the SI (Fig. S3b and SI). High-temperature pyrolysis induced significant morphological changes within the monometallic Co and Ni-MOF. The initial needle-shaped particles transformed into hollow, porous particles (Fig. 2a and b). EDX mapping confirmed the uniform distribution of Co, C, and O, and Ni, C, and O atoms in Co-MOF@850 °C and Ni-MOF@850 °C catalysts (Fig. S4 and SI). Besides, it is to be noticed that increasing the pyrolysis temperature from 550 to 850 °C enlarged the pore size, likely due to the decomposition of the D-cam and 4,4′-Bip ligands, resulting in enhanced porosity. This transformation is expected to increase the specific surface area and expose more active sites, thereby improving the catalytic performance. SEM images for Co and Ni-MOFs pyrolyzed at temperatures ranging from 550 °C to 750 °C are provided in Fig. S5 (SI). PXRD analysis of the Co and Ni-MOF oxides (550–850 °C) revealed significant structural changes during pyrolysis. These changes include the formation of CoO and NiO. In fact, sharp narrow diffraction peaks (Fig. 2c and d) confirmed the high crystallinity of the pyrolyzed monometallic catalysts, with patterns matching the reference values for cubic CoO (JCPDS 00-042-1307) and NiO (JCPDS 47-1049).[37,38] Furthermore, an increase in the intensity of the diffraction peaks was observed with an increase in the pyrolysis temperature, indicating improved crystallinity. The optimized bimetallic CoNi-MOF catalyst also formed hollow porous particles within a size range of 40–58 nm (Fig. 2e and S6b SI). EDX mapping confirmed the uniform distribution of Co, Ni, C, and O atoms (Fig. 2f).

The hollow structure of the bimetallic CoNi composite was further confirmed using scanning transmission electron microscopy (STEM), selected area electron diffraction (SAED) and high-angle annular dark-field scanning transmission electron microscopy (HAADF-STEM) analyses.

The results showed interplanar spacings of 0.24 nm, and 0.25 nm, matching the (111) planes of NiO and CoO, respectively (Fig. 2g, h and S6c, SI). The PXRD pattern of CoNi-MOF@850 °C (Fig. 2i) confirms the presence of CoO and NiO (JCPDS 47-1049) phases. These results confirm the successful formation of the CoO/NiO composite within the carbon matrix and highlight the effective conversion of the bimetallic CoNi-dual-doped MOF into metal-oxide-carbon composites.[39] It is to be noticed that minor diffraction signals were detected in the PXRD spectra of pyrolyzed CoNi-MOF@850 °C, indicating the presence of traces of Co and Ni nanoparticles.

The specific surface area and pore distribution of the mono- and bimetallic Co, Ni, and CoNi-MOFs and their derivatives at 850 °C were investigated using nitrogen adsorption–desorption analysis (Fig. S7a and b, SI). All samples exhibited type-IV isotherms with H3-type hysteresis loops, characteristic of hierarchical mesoporous structures. The CoNi-MOF displayed the highest Brunauer–Emmett–Teller (BET) surface area among the monometallic system, reaching 45.7 $m^2\ g^{-1}$ with a pore size distribution centered at 11.2 nm. Upon pyrolysis, both monometallic Co-MOF@850 °C and Ni-MOF@850 °C showed significant increases in surface area, reaching 124.8 $m^2\ g^{-1}$ and 141.3 $m^2\ g^{-1}$, respectively. Remarkably, the bimetallic CoNi-MOF@850 °C catalyst demonstrated the most pronounced increase, achieving a BET surface area of 183.2 $m^2\ g^{-1}$ and an average pore size of 23.7 nm, thereby surpassing both monometallic systems.

These results highlight the beneficial effect of Ni incorporation in promoting higher porosity and greater surface area.

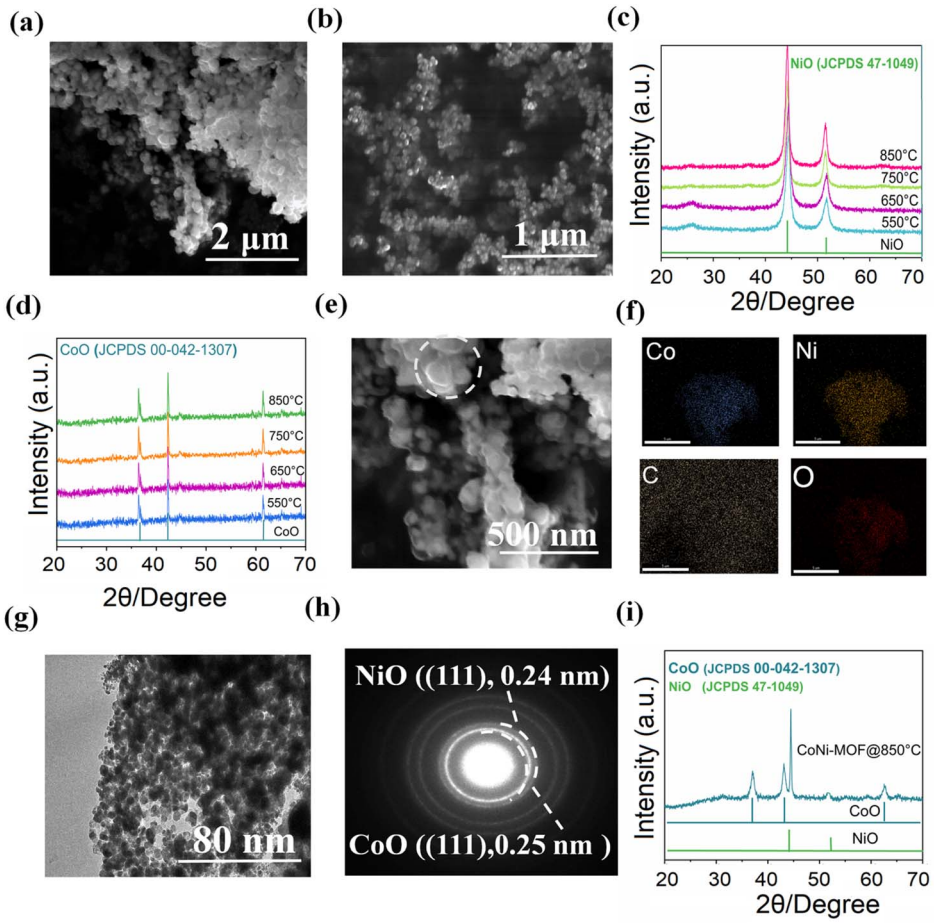

Fig. 2 SEM image of (a) Co-MOF@850 °C, (b) Ni-MOF@850 °C, PXRD patterns for (c) Co, and (d) Ni catalysts pyrolyzed from 550 °C to 850 °C, (e) SEM image of CoNi-MOF@850 °C, (f) the corresponding EDX elemental mapping for CoNi-MOF@850 °C, (g) STEM image for CoNi-MOF@850 °C, (h) SAED pattern for CoNi-MOF@850 °C, and (i) PXRD patterns for pyrolyzed Co, Ni and CoNi-MOF@850 °C catalyst.

We propose that this also leads to an increase in the number of metal active sites and could be a facile route to improve catalytic HER performance. These findings highlight the critical roles of thermal treatment and metal substitution in tailoring the surface properties of these materials.

The BET results are summarized in Table S2 (SI). X-ray photoelectron spectroscopy (XPS) analysis was performed to investigate the chemical composition and electronic structure of the pyrolyzed catalysts.

The XPS survey spectra confirmed the presence of Co, O, and C in the Co catalyst, Ni, O, and C in the Ni catalyst, and Co, Ni, O, and C in the bimetallic CoNi catalyst. These findings are consistent with the EDX elemental mapping results (Fig. S8, SI). As depicted in Fig. 3a and b, the Co 2p spectrum of the Co-MOF@850 °C displays two main peaks at 778.6 eV and 793.3 eV, corresponding to Co $2p_{3/2}$ and Co $2p_{1/2}$ spin–orbit, characteristic of the CoO phase and Co nanoparticles.[40–42] The deconvolution of the Co $2p_{3/2}$ peak revealed a component at 777.3 eV, indicating the presence of metallic Co^0. Additional components at 777.6 eV and 779.8 eV for Co $2p_{3/2}$, and792.8 eV and 793.1 eV for Co $2p_{1/2}$, are attributed to Co^{2+}/Co^{3+}. The presence of Co^{3+}, suggests the surface oxidation of Co^{2+}.

Besides, the presence of satellite peaks at 786.6 eV and 794.8 eV further supports the presence of cobalt oxide. Moreover, the Ni 2p XPS spectrum of the Ni-MOF@850 °C displays two main peaks at 854.2 eV and 871.2 eV, corresponding to the Ni $2p_{3/2}$ and Ni $2p_{1/2}$ spin–orbit, respectively. Deconvolution of the Ni $2p_{3/2}$ region reveals components at 854.1 eV and 855.5 eV, which can be attributed to metallic Ni^0 and Ni^{2+} species. The Ni $2p_{1/2}$ region shows peaks at 870.3 eV and 872.2 eV. A distinct satellite feature observed at 862.7 eV further supports the presence of NiO and metallic Ni nanoparticles.

For the bimetallic CoNi-MOF@850 °C the Co 2p spectrum shows a Co^0 component at 778.1 eV. The peaks at 779.5 eV and 780.9 eV for Co $2p_{3/2}$, and 795.5 eV and 796.3 eV for Co $2p_{1/2}$, along with a satellite band at 784.6 eV, are attributed to Co^{2+}/Co^{3+} species. A weak signal assigned to Co^{3+} was also detected, likely due to the surface oxidation. The Ni 2p XPS spectrum of the CoNi-MOF@850 °C displays two main peaks at 855.2 eV and 872.1 eV, corresponding to the Ni $2p_{3/2}$ and Ni $2p_{1/2}$ spin–orbit components, respectively. Deconvolution of the Ni $2p_{3/2}$ region reveals components at 854.4 eV and 856.5 eV, which can be attributed to metallic Ni^0 and Ni^{2+} species. Likewise, the Ni $2p_{1/2}$ region shows peaks at 871.2 eV and 873.5 eV. A distinct satellite

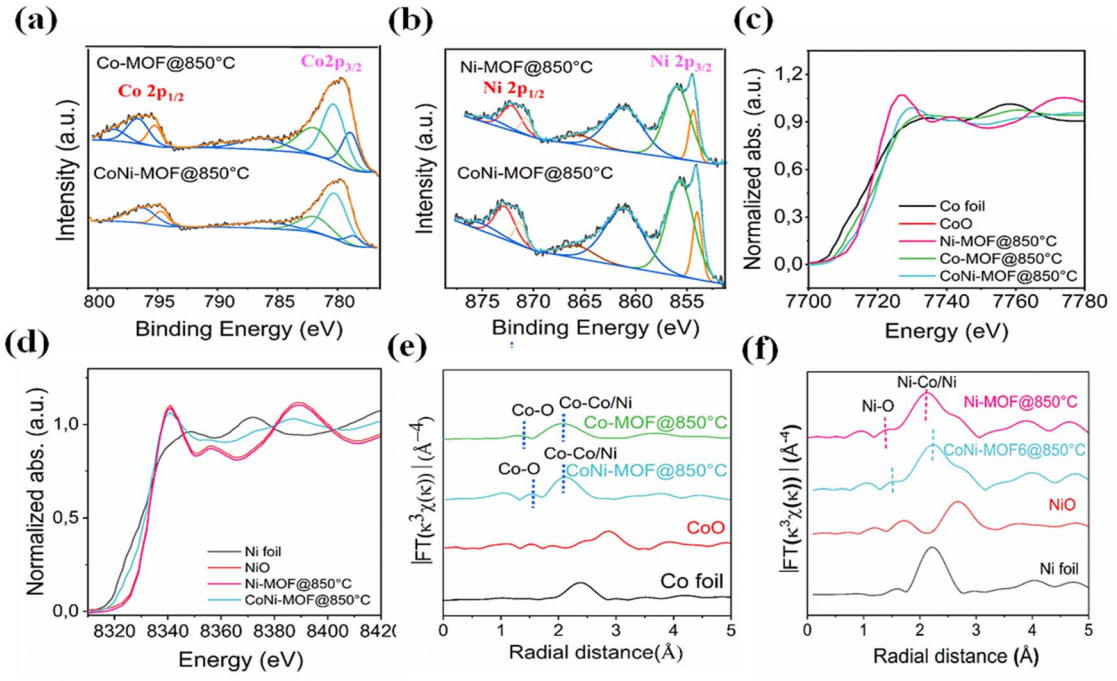

Fig. 3 Deconvoluted high-resolution XPS spectra of (a) Co 2p for Co-MOF@850 °C, and CoNi-MOF@850 °C, (b) Ni 2p for Ni-MOF@850 °C, and CoNi-MOF@850 °C, normalized (c) Co K-edge, (d) Ni K-edge XANES spectra of Co, Ni, and CoNi-MOF@850 °C, compared with corresponding Co and Ni reference compounds, (e) Co K-edge and (f) Ni K-edge EXAFS R-space spectra of Co, Ni and CoNi oxides, along with standard Co and Ni reference materials.

feature observed at 861.1 eV further supports the presence of NiO and metallic Ni nanoparticles.[43–45]

To gain deeper insights into the oxidation states and coordination environments of Co and Ni in the investigated oxide catalysts, X-ray absorption spectroscopy (XAS), including X-ray absorption near-edge structure (XANES) and extended X-ray absorption fine structure (EXAFS) analyses, was performed.[46] As presented in Fig. 3c, the Co K-edge XANES spectra of Co and CoNi oxides exhibit an absorption edge located between the metallic Co foil and CoO, indicating an average Co oxidation state between 0 and +2. Similarly, the Ni K-edge XANES spectra of Ni and CoNi oxides suggest that Ni oxide shows an absorption edge between the metallic Ni-foil and NiO, indicating an average oxidation state between 0 and +2 (Fig. 3d).[47] The Co K-edge EXAFS spectra of Co and CoNi oxides (Fig. 3e) revealed two prominent peaks: the first at 1.51 Å, corresponding to Co–O bonds, and the second at 2.04 Å, associated with Co–M (M = Co, Ni) interactions. Upon Ni incorporation, a noticeable increase in bond lengths was observed, with the Co–O distance extending to 1.54 Å and the Co–M distance increasing to 2.2 Å. Similarly, the Ni K-edge EXAFS spectra of Ni and CoNi oxides display two distinct peaks: one at 1.58 Å and 1.59 Å, attributed to Ni–O bonds, and a second peak at 2.41 Å and 2.45 Å, corresponding to Ni–M (M = Co, Ni) coordination, respectively (Fig. 3f). The positive shift of Co K-edge and Ni K-edge in the CoNi-MOF@850 °C indicates structural expansion of the cobalt oxide lattice, which can be attributed to the larger atomic/ionic radius of Ni compared to Co, leading to a lattice distortion and expansion upon substitution.[48] The Fourier-transformed *k*-space EXAFS profiles of Co and Ni K-edges for Co, Ni, and CoNi catalysts are depicted in Fig. S9 (SI). The XAS results are in good agreement with the structural features obtained from XPS.

ICP-OES results for the Co, Ni, and NiFeMOFs, and pyrolyzed Co, Ni and CoNi-MOF@850 °C are summarized in Table S3 (SI).

Electrocatalytic activity

The electrocatalytic HER performances of all investigated catalysts were first investigated in an Ar-saturated 1 M aqueous KOH electrolyte solution using a typical three-electrode setup. The electrocatalytic activities of all catalysts pyrolyzed at different temperatures were studied and compared with that of commercial Pt/C (10 wt% Pt) as a reference compound under the same conditions. All the potentials were referenced to the reversible hydrogen electrode (RHE) (see SI). Fig. 4a and b present the LSV curves of Co-MOF and Ni-MOF catalysts pyrolyzed at different temperatures, respectively. Among the Co-based catalysts, Co-MOF@850 °C exhibited the highest activity, requiring an overpotential of 239 mV at 10 mA cm^{-2} with a Tafel slope of 122 mV dec^{-1} (Fig. S10, SI). Likewise, Ni-MOF@850 °C surpassed all Ni-MOF samples pyrolyzed at lower temperatures, delivering an overpotential of 172 mV at 10 mA cm^{-2} and a Tafel slope of 116 mV dec^{-1} (Fig. S11, SI). These results indicate that pyrolysis at 850 °C enhances the HER activity by generating more active sites, highlighting the critical role of temperature in optimizing the HER.[49,50] To enhance the catalytic kinetics, Ni was doped with Co to form bimetallic CoNi-MOF crystals, which were pyrolyzed at the optimized temperature. Electrochemical

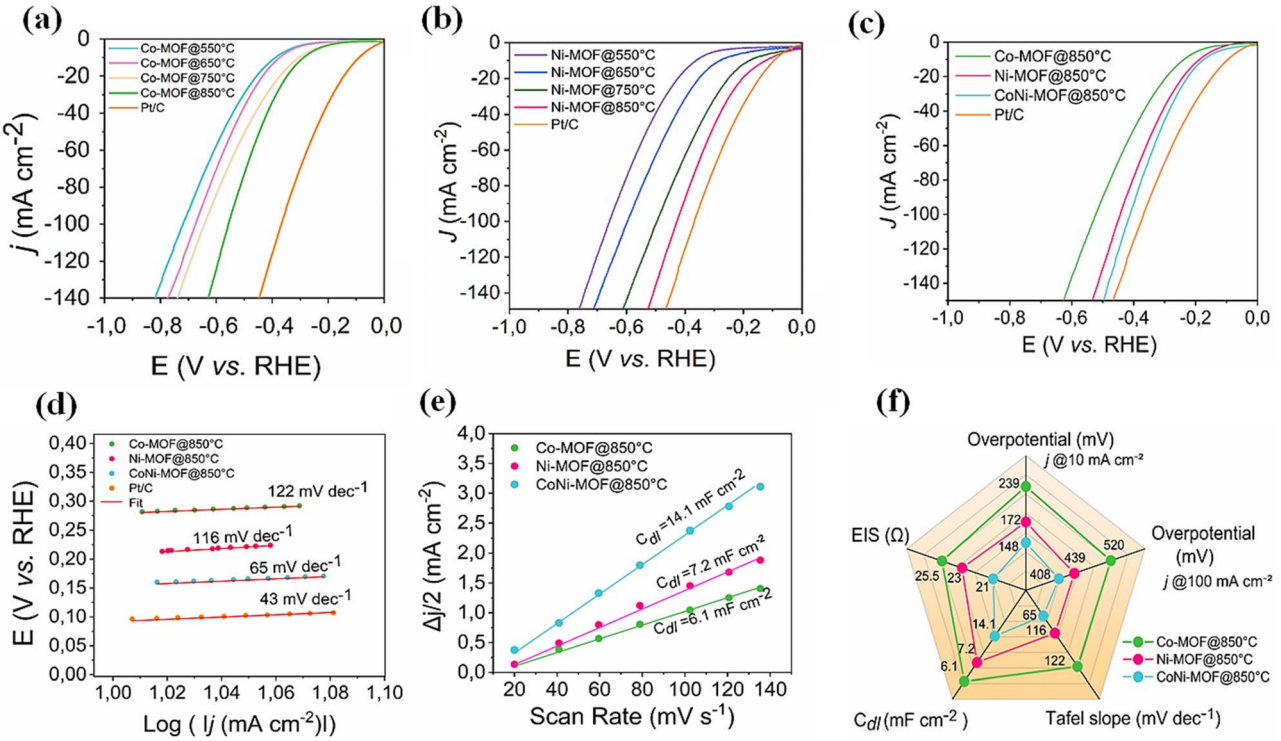

Fig. 4 LSV curves of (a) Co-MOF catalysts pyrolyzed at different temperatures, (b) Ni-MOF catalysts pyrolyzed at different temperatures, (c) Co, Ni, and CoNi-MOF@850 °C catalysts measured in 1 M aqueous KOH medium without *iR* correction, (d) Tafel slope of Co, Ni, CoNi catalysts measured at $j = 10$ mA cm-2, (e) C_{dl} plot s of Co, Ni and CoNi catalysts, and (f) summary of the catalytic performance of Co, Ni, and CoNi-MOF@850 °C.

evaluations under identical conditions as the monometallic system confirmed that CoNi-MOF@850 °C exhibited superior catalytic activity compared with its monometallic Co and Ni systems. It required an overpotential of 148 mV to achieve a current density of 10 mA cm^{-2}, which is slightly higher than that of 10% Pt/C (95 mV) (Fig. 4c). These results also demonstrate that CoNi-MOF@850 °C can be considered one of the most efficient porous CoNi-MOF-derived HER catalysts.[50–53]

The Tafel slopes derived from the LSV curves revealed that the optimized CoNi-MOF@850 °C catalyst exhibited a lower Tafel slope of 65 mV dec^{-1} compared to 122 mV dec^{-1} for the Co-MOF@850 °C and 140 mV dec^{-1} for the Ni-MOF@850 °C monometallic system (Fig. 4d). In alkaline media, the HER mechanism follows either the Volmer–Tafel or Volmer–Heyrovsky pathways. The initial Volmer step involves dissociation of water at the electrode surface, generating adsorbed hydrogen atoms (H_{ads}). These atoms either recombine in the Tafel step ($H_{ads} + H_{ads} \rightarrow H_2$) or react with water in the Heyrovsky step ($H_{ads} + H_2O + e^- \rightarrow H_2 + OH^-$). Tafel slopes above 120 mV dec^{-1} indicate that water dissociation (Volmer step) is the rate-limiting step, whereas lower values suggest faster kinetics. This suggests that Ni doping alters the HER mechanism by shifting it toward the Volmer–Heyrovsky pathway, thereby improving the reaction kinetics. The bimetallic CoNi catalyst also outperforms previously reported catalysts, including CoNiP/CoNi system,[51] NiCoP alloy,[52] and Co–Ni phosphide nanowires (CoNiP-NWs).[53] These findings highlight the significant catalytic enhancement achieved by Ni-doping.

Electrochemical impedance spectroscopy (EIS) studies were conducted to examine the interfacial properties and charge transfer resistance between the electrode and the electrolyte. The arc radius in EIS Nyquist plots is commonly used as an indicator of the charge transfer rate, where a smaller arc radius suggests a lower charge-transfer resistance.

As presented in Fig. S12a, (SI) the bimetallic CoNi-MOF@850 °C exhibited the smallest arc radius, compared to the monometallic Co-MOF@850 °C and Ni-MOF@850 °C catalysts, indicating more efficient charge transfer at the electrode/electrolyte interface, which enhanced its HER kinetics. Based on the fitting of the Nyquist plots, the charge-transfer resistance (R_{ct}) of CoNi-MOF@850 °C was found to be 21 Ω, which is significantly lower than that of Co-MOF@850 °C (25.2 Ω) and Ni-MOF@650 °C (23 Ω), The lowest R_{ct} value for CoNi-MOF@850 °C reflects its superior interfacial electron transfer during the HER. These results further confirmed that Ni doping in Co-MOF significantly improved the interfacial electron transfer, reducing the charge-transfer resistance (Fig. S12b, SI).

Cyclic voltammetry in the non-faradaic region demonstrated increased intrinsic catalytic activity, as evidenced by the higher current density observed for CoNi-MOF@850 °C compared to the monometallic Co and Ni-MOF@850 °C, indicating enhanced intrinsic catalytic activity. Additionally, the higher double-layer capacitance Cdl of CoNi-MOF@850 °C (14.1 mF

cm^{-2}) compared to that of Co and Ni (6.1 mF cm^{-2}, and 7.2 mF cm^{-2}, respectively) indicates a greater number of exposed active sites.

This highlights the superior charge transfer, active site accessibility, and overall electrocatalytic efficiency of the bimetallic composite, making it a promising candidate for HER applications (Fig. 4e and S13, SI)). Fig. 4f reports a summary of the catalytic performance of the monometallic Co, Ni, and bimetallic CoNi-MOF@850 °C.

Mechanistic studies and catalytic mechanism

To evaluate the long-term durability of the best-performing CoNi@850 °C catalyst toward the HER, continuous cyclic voltammetry (CV) tests were carried out for 1000 cycles at a scan rate of 50 mV s^{-1} in 1 M KOH. Subsequent LSV measurements revealed a slight increase of the Tafel slope, indicative of minor activation and enhanced HER kinetics (Fig. S14, SI).[22,53]

The stability of the bimetallic catalyst was further examined by chronoamperometry (*ca*). As shown in Fig. 5a, the investigated catalyst maintained 97.8% of its initial current density after 24 h of continuous operation at a constant overpotential of 113 mV. These results were further confirmed by the LSV curves obtained before and after the stability test (Fig. 5b).

Hydrogen production was quantified using gas chromatography (Fig. 5c), revealing a high faradaic efficiency (FE) of 98.6% for the bimetallic CoNi-MOF@850 °C catalyst. The time-dependent GC measurements show that the amount of evolved H_2 increases steadily during 24 h of chronoamperometry test till reaching approximately 1570 nmol. This continuous rise correlates with the stable current density maintained during long-term operation, demonstrating that the catalyst preserves its intrinsic electrocatalytic activity without noticeable degradation. Overall, the nearly quantitative faradaic

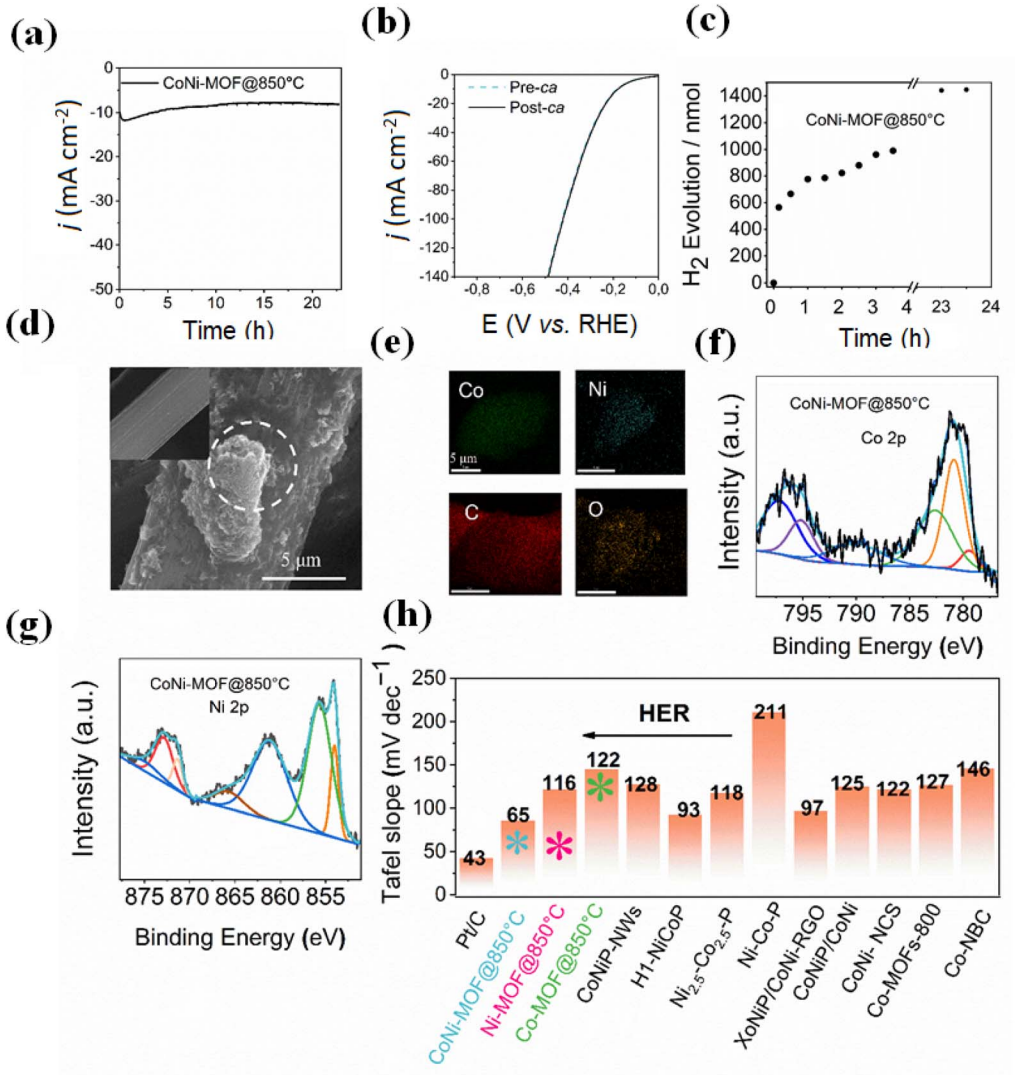

Fig. 5 (a) Stability test curve measured for CoNi-MOF@850 °C, (b) LSV curves before and after *ca* test, (c) time-dependent hydrogen evolution of the bimetallic CoNi-MOF@850 °C, (d) post-HER SEM images (insert: SEM image of carbon paper) measured for CoNi-MOF@850 °C catalyst, (e) the corresponding EDX elemental mapping of CoNi-MOF@850 °C, post-HER-XPS survey spectra of (f) Co 2p (g) Ni 2p for CoNi-MOF@850 °C, and (h) performance comparison of the investigated catalysts with the best-performing HER catalysts reported in the literature.

efficiency confirms the excellent stability and selectivity of the catalyst under sustained HER conditions.

To assess the mechanistic robustness of the catalyst under operational conditions, post-catalysis SEM-EDX analysis confirmed that the hollow particle morphology of the bimetallic catalyst was preserved even after 24 h of operation, highlighting its structural stability (Fig. 5d and e). Moreover, the homogeneous distribution of Co and Ni elements was maintained, indicating the absence of significant leaching during HER. These observations were further corroborated by ICP-OES analysis of the post-electrolysis electrolyte, which revealed only trace amounts of dissolved metals, confirming that Co and Ni leaching was minimal under applied HER conditions.

XPS analysis performed after catalysis (Fig. 5f and g) confirm that the surface chemistry of the catalyst remains largely preserved. The spectra clearly show the continued presence of CoO and NiO as the dominant surface phases, along with detectable traces of metallic Co^0 and Ni^0. This retention of both oxide and metallic species demonstrates that the active sites remain chemically stable throughout the HER operation.

These results suggest that the CoNi-MOF catalyst maintains its structural and catalytic properties over prolonged HER operation. Comparison of HER activities of different dual CoNi catalysts is presented in Fig. 5h and Table S4, (SI).

These mechanistic insights are supported by Density Functional Theory (DFT) studies reported for comparable bimetallic CoNi oxide systems.[57,58] In fact, these calculations reveal that the incorporation of Ni into Co-based oxides modulates the d-band center and lowers the hydrogen adsorption free energy ($\Delta G(H^*)$) toward more energetically favorable states, thereby enabling balanced H* adsorption on Co sites and promoting efficient H_2 desorption on adjacent Ni sites. Theoretical models further highlight the critical role of oxygen vacancies and metal–oxygen interactions, which increase the density of active sites and strengthen the electronic interaction within the bimetallic framework. Based on these findings, the experimental results and theoretical studies demonstrate that the synergistic combination of CoO/NiO composite and enhanced electronic coupling improves the charge transport, optimizes the ΔG_{H^*}, and enables the excellent HER activity and long-term stability of the CoNi-MOF@850 °C catalyst.[59]

Alkaline hydrogen evolution in an AEM electrolyzer

To evaluate the practical applicability of CoNi-MOF@850 °C as an efficient catalyst under industrially relevant conditions, an anion exchange membrane (AEM) alkaline electrolyzer was assembled. The device, with a geometric active area of 2 cm^2, employed a conventional sandwich-type configuration comprising current collectors, the CoNi-MOF@850 °C catalyst coated onto carbon paper as the cathode, commercial Ni foam as the anode, and a pre-activated AEM separator. The cathode catalyst loading was set at 0.6 mg cm^{-2}, and 1 M KOH electrolyte was continuously circulated through the flow channels using a peristaltic pump to ensure uniform ion transport and minimize concentration gradients. A schematic illustration of the electrolyzer setup is shown in Fig. 6a.

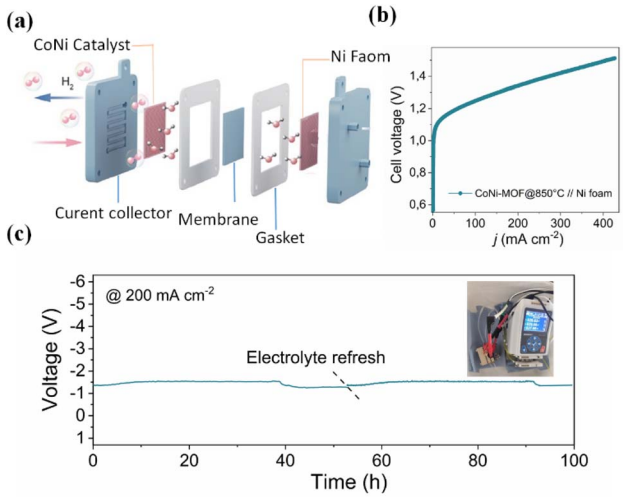

Fig. 6 (a) Schematic illustration of the AEM electrolyzer configuration. (b) LSV curve of the CoNi-MOF@850 °C//Ni foam device at a current density of 200 mA cm^{-2}. (c) Long-term stability test of the CoNi-MOF@850 °C//Ni foam electrolyzer operated at 200 mA cm^{-2} and 70 °C in 1 M KOH. The inset shows a photograph of the AEM device under operating conditions.

Remarkably, the CoNi-MOF@850 °C//Ni foam system required only 1.34 V to achieve a high current density of 200 mA cm^{-2} (Fig. 6b), highlighting its outstanding catalytic efficiency. Moreover, long-term stability test demonstrated the excellent stability of the catalyst, with ~96% potential retention maintained over 100 h at 200 mA cm^{-2} without observable performance decay (Fig. 6c). These findings establish the bimetallic CoNi-MOF@850 °C as a robust and highly efficient cathode catalyst for practical hydrogen production under industrially relevant conditions.

Based on these findings, the remarkable HER performance of the bimetallic CoNi-MOF@850 °C compared to that of monometallic Co and Ni catalysts can be attributed to several key factors: (i) enhanced porosity and conductivity, In fact, pyrolysis at 850 °C generates a highly porous architecture with a large surface area and interconnected pores, increasing the number of active sites and improving electrical conductivity. (ii) Hollow structure benefits: The unique hollow morphology enhances electrolyte contact, facilitates gas bubble release, and significantly improves the catalyst stability. (iii) Synergistic Co–Ni interaction: Ni doping introduces additional active sites, and the interaction between Co and Ni optimizes the adsorption energies of the reaction intermediates, lowering the kinetic barriers. (iv) Facilitated water dissociation: The Co–Ni–O system enhances water dissociation, which is a key step in the alkaline HER, thereby improving the overall reaction kinetics.[54–56] In fact, the synergy of Co and Ni plays a crucial role in boosting the HER efficiency. Ni sites promote OH* desorption during water dissociation, whereas Co sites enhance the recombination of adsorbed hydrogen for H_2 generation. Additionally, the formation of CoNi-oxide improved the electrical conductivity, ensuring efficient charge transfer. This cooperative interaction between Co and Ni in their oxide and metallic states lowered the

kinetic barriers for water dissociation and hydrogen desorption, making the bimetallic CoNi-MOF@850 °C an efficient HER catalyst.[60–63]

Conclusions

In summary, we have studied a series of hierarchical hollow monometallic and bimetallic CoNi dual-doped carbon electrocatalysts through the rational design and pyrolysis of novel mixed-ligand MOF. Among all catalysts, the bimetallic CoNi-MOF@850 °C obtained at a carefully optimized pyrolysis temperature of 850 °C, demonstrated exceptional catalytic performance, achieving a low overpotential of 148 mV at a current density of 10 mA cm^{-2} in 1 M KOH, outperforming the monometallic Co and Ni catalysts. Impressively, the CoNi-MOF@850 °C//Ni foam system demonstrated excellent stability in an AEM electrolyzer, maintaining ~96% potential retention over 100 h at 200 mA cm^{-2}. This superior activity is attributed to the synergistic interaction between Co and Ni in the bimetallic structure, which enhances the electronic properties, facilitates charge transfer, and increases the density of the active sites. Additionally, the unique hierarchical hollow architecture, formed through the controlled pyrolysis of MOF provides a high surface area, abundant active sites, and improved mass diffusion. These findings highlight the significant promise of MOF-derived bimetallic catalysts as efficient and cost-effective alternatives to noble-metal-based electrocatalysts for sustainable hydrogen production.

Conflicts of interest

There are no conflicts of interest to declare.

Data availability

CCDC 2471448 contains the supplementary crystallographic data for this paper.[64]

Data for this article, including spectroscopic, catalytic and analytical data are available at zenodo.org at URL – format https://doi.org/10.5281/zenodo.16572110. Additional data supporting this article have been included as part of the supplementary information (SI). Supplementary information: experimental procedures, spectroscopic, catalytic, and analytical data. See DOI: https://doi.org/10.1039/d5se01348h.

Acknowledgements

The authors gratefully acknowledge financial support from the Alexander von Humboldt Foundation for postdoctoral fellowships (project no. D. A: 1235340, S. A. C: 1214642, R. L: 1186323, S.R:1229071). T. R. S. and C. S. acknowledge financial support from the Deutsche Forschungsgemeinschaft DFG (project no 364549901, 510966757); R. L, C. N., D. G and C. S. gratefully acknowledge financial support provided by the Carl Zeiss Foundation (Breakthrough Project "Halocycles, project ID: P2021-10-007)). Mr Marco Santucci (Johannes Gutenberg University Mainz) is gratefully acknowledged for STEM measurements. Mr Leon Prädel (Max Planck-Institute for Polymer Research, Mainz) is gratefully acknowledged for XPS measurements. C. S. gratefully acknowledges financial support provided by the Gutenberg Research College, and the Top-Level Research Area SusInnoScience.

References

1 N. Jiang, Y. Cao, H. Cong, Q. Ge, W. Zhao and B. You, *ACS Appl. Mater. Interfaces*, 2025, **17**, 5648–5670.
2 S. Chen, J. Xu, J. Chen, Y. Yao and F. Wang, *Small*, 2024, **20**, 1–14.
3 X. Huo, J. Huang, M. Gao, W. Zhu, W. Liu, Q. Liu, L. Cao, K. Kajiyoshi, Y. Zhao, Y. Liu, Z. Li and Y. Feng, *ACS Appl. Energy Mater.*, 2024, **7**, 2862–2871.
4 T. Chen, Q. Guo, J. Ye, Q. Jiang, N. Chai and F. Y. Yi, *ACS Appl. Nano Mater.*, 2025, **8**(6), 2730–2740.
5 S. A. Chala, R. Liu, E. O. Oseghe, S. T. Clausing, C. Kampf, J. Bansmann, A. H. Clark, Y. Zhou, I. Lieberwirth, J. Biskupek, U. Kaiser and C. Streb, *ACS Catal.*, 2024, **14**, 15553–15564.
6 Z. Chen, W. Cheng, K. Cao, M. Jin, S. Rahali, S. A. Chala, E. Ebrahimi, N. Ma, R. Liu, K. Lakshmanan, C. Y. Chang, C. C. Cheung, H. Luo, Y. Wang, B. J. Hwang and C. Streb, *Small*, 2024, 1–11.
7 Y. Zhao, D. Gao, J. Biskupek, U. Kaiser and R. Liu, *Mater. Adv.*, 2024, **5**, 4786–4793.
8 W. Shen, J. Cui, C. Chen, L. Zhang and D. Sun, *J. Colloid Interface Sci.*, 2024, **659**, 364–373.
9 Q. Li, F. Huang, S. Li, H. Zhang and X. Y. Yu, *Small*, 2022, **18**, 1–11.
10 K. J. Vetti and A. Koca, *Int. J. Hydrogen Energy*, 2025, **97**, 214–225.
11 K. Gothandapani, G. Tamil Selvi, R. Sofia Jennifer, V. Velmurugan, S. Pandiaraj, M. Muthuramamoorthy, S. Pitchaimuthu, V. Raghavan, A. C. Josephine Malathi, A. Alodhayb and A. Nirmala Grace, *Int. J. Hydrogen Energy*, 2024, **52**, 1164–1171.
12 Y. Chang, P. Zhai, J. Hou, J. Zhao and J. Gao, *Adv. Energy Mater.*, 2022, **12**, 2102359.
13 J. Diao, Y. Qiu, S. Liu, W. Wang, K. Chen, H. Li, W. Yuan, Y. Qu and X. Guo, *Adv. Mater.*, 2020, **32**, 1905679.
14 X. Guo, Z. Liu, F. Liu, J. Zhang, L. Zheng, Y. Hu, J. Mao, H. Liu, Y. Xue and C. Tang, *Catal. Sci. Technol.*, 2020, **10**, 1056–1065.
15 J. Li, Q. Zhuang, P. Xu, D. Zhang, L. Wei and D. Yuan, *Chin. J. Catal.*, 2018, **39**, 1403–1410.
16 Y. Liu, X. Liu, A. R. Jadhav, T. Yang, Y. Hwang, H. Wang, L. Wang, Y. Luo, A. Kumar, J. Lee, H. T. D. Bui, M. G. Kim and H. Lee, *Angew. Chem., Int. Ed.*, 2022, **134**, 1–10.
17 B. Zhao, Y. Wang, J. Che, L. Xiong, D. Gao and D. Chen, *ACS Appl. Mater. Interfaces*, 2025, **17**, 30978–30987.
18 R. Li, X. Chen, Z. Bian, R. Yu, Y. Chen, J. Zhang, J. Wang and X. Feng, *J. Alloys Compd.*, 2025, **1020**, 179345.
19 S. Li, J. Yu, Q. Liu, J. Liu, D. Song, J. Zhu, R. Li and J. Wang, *Carbon*, 2025, **235**, 120098.

20 K. Chi, X. Tian, Q. Wang, Z. Zhang, X. Zhang, Y. Zhang, F. Jing, Q. Lv, W. Yao, F. Xiao and S. Wang, *J. Catal.*, 2020, **381**, 44–52.
21 X. Wang, Y. Zhang, H. Si, Q. Zhang, J. Wu, L. Gao, X. Wei, Y. Sun, Q. Liao, Z. Zhang, K. Ammarah, L. Gu, Z. Kang and Y. Zhang, *J. Am. Chem. Soc.*, 2020, **142**, 4298–4308.
22 Z. Wang, H. Liu, R. Ge, X. Ren, J. Ren, D. Yang, L. Zhang and X. Sun, *ACS Catal.*, 2018, **8**, 2236–2241.
23 Y. Song, J. Cheng, J. Liu, Q. Ye, X. Gao, J. Lu and Y. Cheng, *Appl. Catal., B*, 2021, **298**, 120488.
24 H. F. Wang, L. Chen, H. Pang, S. Kaskel and Q. Xu, *Chem. Soc. Rev.*, 2020, **49**, 1414–1448.
25 Y. Lu, Z. Zhao, X. Liu, X. Yu, W. Li, C. Pei, H. S. Park, J. K. Kim and H. Pang, *Adv. Sci.*, 2025, **12**, 1–14.
26 A. Said, B. Qian, R. Zhang, C. Yang, K. Xu, K. Chen and D. Xue, *Electrochim. Acta*, 2025, **534**, 146577.
27 Q. Zhang, Y. Miao, Y. Xiao, J. Hu, H. Gong and Q. Zeng, *Inorg. Chem. Front.*, 2025, **12**, 1935–1949.
28 Y. Wang, Y. Fan and Y. Z. Chen, *J. Mater. Chem. A*, 2025, **13**, 10892–10898.
29 X. Y. Chen, Z. A. Hu, Y. Qu, R. J. Ning, W. Da Tao, S. Q. He, Z. F. Liu, Y. H. Shen and L. Qin, *CrystEngComm*, 2025, **27**, 1591–1598.
30 H. Jiang, Z. Zhao, G. Li, M. Wang, P. Chen, X. Liu, X. Tu, Y. Hu, Z. Shen and Y. Wu, *Adv. Sci.*, 2024, **11**, 2306919.
31 M. A. Ehsan, M. Akilarasan, W. Farooq, S. M. Al-Mansour and A. S. Hakeem, *Energy Fuels*, 2025, **7**(12), 3835–3843.
32 V. S. R. Channu, R. Holze and B. Rambabu, *Colloids Surf., A*, 2012, **414**, 204–208.
33 M. Linares-Moreau, L. A. Brandner, M. de J. Velásquez-Hernández, J. Fonseca, Y. Benseghir, J. M. Chin, D. Maspoch, C. Doonan and P. Falcaro, *Adv. Mater.*, 2024, **36**, 1–10.
34 E. Aubert, M. Abboud, A. Doudouh, P. Durand, P. Peluso, A. Ligresti, B. Vigolo, S. Cossu, P. Pale and V. Mamane, *RSC Adv.*, 2017, **7**, 7358–7367.
35 E. Zeini Jahromi and J. Gailer, *Dalton Trans.*, 2010, **39**, 329–336.
36 Q. Wu, J. Liang, D. Wang, R. Wang and C. Janiak, *Chem. Soc. Rev.*, 2024, **53**, 601–622.
37 P. Arunkumar, S. Gayathri and J. H. Han, *ACS Appl. Energy Mater.*, 2022, **5**, 2975–2992.
38 M. S. Wu, Y. R. Zheng and G. W. Lina, *Chem. Commun.*, 2014, **50**, 8246–8248.
39 P. Arunkumar, S. Gayathri and J. H. Han, *ChemSusChem*, 2021, **14**, 1921–1935.
40 R. Cheng, Z. Liu, P. Manasa, Z. Zhao, H. Pan, F. Xu, L. Sun and F. Rosei, *Int. J. Hydrogen Energy*, 2025, **102**, 375–385.
41 M. Li, Z. Xie, J. Liu, J. Ni, M. Deng, Y. Tu, S. Jiang, J. Liu, G. Chen, L. Li and Z. Wei, *J. Phys. Chem. C*, 2025, **129**(6), 3031–3039.
42 J. Zhu, J. Chi, T. Cui, T. Wang, L. Guo, X. Liu, J. Lai, Z. Wu and L. Wang, *Adv. Funct. Mater.*, 2024, **34**, 1–11.
43 L. Wang, L. Song, Z. Yang, Y. M. Chang, F. Hu, L. Li, L. Li and H. Y. Chen, *Adv. Funct. Mater.*, 2023, **33**, 1–10.
44 L. Ma, I. Jia, X. Guo and L. Xiang, *Chin. J. Catal.*, 2014, **35**, 108–119.
45 H. Yang, F. Chen, X. Wang, J. Qian, J. Wang, J. Li, C. Lv, L. Li, S. Bandaru and J. Gao, *Adv. Funct. Mater.*, 2025, **34**, 1–13.
46 L. M. Toscani, M. G. Zimicz, T. S. Martins, D. G. Lamas and S. A. Larrondo, *RSC Adv.*, 2018, **8**, 12190–12203.
47 D. Gajdek, P. A. T. Olsson, S. Blomberg, J. Gustafson, P. A. Carlsson, D. Haase, E. Lundgren and L. R. Merte, *J. Phys. Chem. C*, 2022, **126**, 3411–3418.
48 S. Ajmal, A. Rasheed, W. Sheng, G. Dastgeer, Q. A. T. Nguyen, P. Wang, P. Chen, S. Liu, V. Q. Bui, M. Zhu, P. Li and D. Wang, *Adv. Mater.*, 2024, **34**, 1–14.
49 Y. A. Attia, M. Taha and S. H. Abdel-Hafez, *New J. Chem.*, 2025, **49**, 1854–1864.
50 S. Huang, A. Huang, H. Huang, C. Tan, Y. Yang, W. Tang, L. Hao, X. Xu and S. Agathopoulos, *ACS Appl. Mater. Interfaces*, 2025, **17**(36), 50103–50121.
51 H. Shi, T. Y. Dai, X. Y. Sun, Z. L. Zhou, S. P. Zeng, T. H. Wang, G. F. Han, Z. Wen, Q. R. Fang, X. Y. Lang and Q. Jiang, *Adv. Mater.*, 2024, **34**, 1–12.
52 B. Yan, X. Qin, T. Chen, Z. Teng, D. K. Cho, H. W. Lim, H. Hong, Y. Piao, L. Xu and J. Y. Kim, *Adv. Funct. Mater.*, 2024, **34**, 1–11.
53 M. A. Chandran, S. Sahoo, A. K. Singh and B. L. V. S. Prasad, *Small*, 2024, 1–12.
54 J. Zhang, M. Gao, Y. Wang, Y. Wei, Y. Qi, Q. Liu, X. Li, Q. Ma, J. Huang and Y. Feng, *Nanoscale*, 2024, **16**, 2193–2199.
55 M. Abitha, C. Viswanathan and N. Ponpandian, *Sustainable Energy Fuels*, 2025, **9**, 921–941.
56 L. Zhu, Y. Cheng and Y. Gong, *Int. J. Hydrogen Energy*, 2025, **97**, 1177–1186.
57 P. Zhang, J. Zhang, Y. Kong, S. Chen, D. Pan, B. Wang, D. Fan and X. Li, *ACS Appl. Energy Mater.*, 2025, **8**, 9379–9390.
58 H. Hao, J. Wang, Z. Wang, J. Li, Z. Jian, B. Liu, S. Shen, L. Xu, Z. Lv and B. Wei, *Nano Energy*, 2025, **141**, 111125.
59 J. Deng, P. Ren, D. Deng and X. Bao, *Angew. Chem., Int. Ed.*, 2015, **54**, 2100–2104.
60 S. Ahmad, M. Egilmez, R. Shanmugam, W. Abuzaid, S. Sharma, R. R. Gangavarapu, F. Mustafa, S. El-Khatib, H. Alawadhi and A. M. Kannan, *ACS Appl. Energy Mater.*, 2023, **6**, 10652–10664.
61 Y. Du, M. Zhang, Z. Wang, Y. Liu, Y. Liu, Y. Geng and L. Wang, *J. Mater. Chem. A*, 2019, **7**, 8602–8608.
62 Z. Cai, A. Wu, H. Yan, Y. Xiao, C. Chen, C. Tian, L. Wang, R. Wang and H. Fu, *Nanoscale*, 2018, **10**, 7619–7629.
63 R. Madhu, J. Muthukumar, P. Arunachalam, P. Gudlur and S. Kundu, *J. Phys. Chem. C*, 2024, **128**, 12891–12902.
64 CCDC 2471448: Experimental Crystal Structure Determination, 2025, DOI: 10.5517/ccdc.csd.cc2nyr4j.